Investigation of a Novel Thermochemical Reactor for Medium- and Low-Temperature Heating Applications in Buildings

Xiaojing Han [1] , Cheng Zeng [2,*] , Zishang Zhu [3], Yanyi Sun [3] and Xudong Zhao [2]

[1] College of Civil Engineering, Taiyuan University of Technology, Taiyuan 030024, China; xiaojing910105@163.com
[2] Energy and Environment Institute, University of Hull, Hull HU6 7RX, UK; xudong.zhao@hull.ac.uk
[3] Department of Civil Engineering, Surveying and Construction Management, Kingston University London, London KT2 7LB, UK; zishang.zhu@hull.ac.uk (Z.Z.); y.sun@kingston.ac.uk (Y.S.)
* Correspondence: c.zeng@hull.ac.uk

Abstract: This research paper investigates a novel triangular honeycomb thermochemical energy storage reactor for low- and medium-temperature applications in buildings, emphasizing its potential to enhance sustainable heating. Using a validated 3D numerical model, the reactor's performance is analyzed in depth across various configurations, focusing on key parameters such as energy storage density, pressure drop, internal air flow distribution, and round-trip efficiency. Results show that the reactor achieved an energy storage density of 872 kJ/kg and a round-trip thermal efficiency of 41.51% under optimal conditions. Additionally, the triangular honeycomb reactor (30°, 60, and 90°) configuration achieved the highest temperature lift of 48.7 °C. In a feasibility analysis for residential heating in northern China, the reactor with 30°, 60°, and 90° angles required 24.91% less volume to meet daily heating demands compared to other configurations. This study contributes valuable insights for the development of efficient, low-carbon heating solutions for low- and medium-temperature applications in buildings, offering interesting advancements in the field of thermochemical energy storage technology.

Keywords: thermochemical energy storage; reactor; parameter study; low- and medium-temperature application

1. Introduction

1.1. The Need to Use Sustainable Measures in Medium- and Low-Temperature Heating

Low-carbon heating in the medium- and low-temperature range, with a flow temperature range of 30 °C to 65 °C, is critical for the decarbonization of the operational carbon emissions of buildings. A viable strategy is to effectively utilize and store low-carbon renewable energy, such as solar energy, off-peak renewable electricity, and industrial waste heat, to meet space heating demands as required, especially during winter or cold nights. But the intermittent nature of renewable energy sources, including solar energy, off-peak electricity, and industrial waste heat, poses significant challenges to their widespread adoption [1]. However, the emergence of thermal energy storage technology offers a promising solution to address the temporal mismatch between energy supply and residential heating demands in building applications [2]. Several solutions are currently commercially available, including thermal storage cylinders integrated with immersion heaters, heat pumps, or solar thermal modules, as well as the utilization of battery storage for residential, commercial, and utility purposes. Despite the availability of these promising solutions, attention should also be directed towards emerging technologies still in the developmental stage, such as adsorption-based thermochemical energy storage.

Among various thermal energy storage technologies, adsorption-based thermochemical energy storage stands out as particularly promising due to its high energy storage density and minimal heat loss during long-term seasonal storage periods. In this process,

thermal energy is captured and stored as adsorption potential during the charging phase, as the adsorbates are desorbed from the adsorbent. Subsequently, during the discharging phase, the adsorbent reabsorbs the adsorbates, releasing the stored energy in the form of adsorption heat. This released energy can then be utilized to provide space heating and hot tap water in residential building environments [3].

When compared to battery storage, adsorption-based technology presents a distinct advantage by not requiring the environment to be maintained at a temperature suitable for battery operations. This is particularly beneficial, given that battery performance in winter tends to diminish and relies heavily on ideal external conditions for long-term durability and optimal performance. In contrast to sensible energy storage methods like thermal storage cylinders, adsorption-based energy storage offers significantly higher energy density, typically ranging from 2 to 10 times greater. This heightened energy density stems from the chemical potential inherent in adsorption processes, allowing for more energy to be stored within the same volume. Furthermore, during storage, adsorption-based systems experience minimal energy loss, as the stored energy is bound within the chemical bonds of the adsorbent material. Unlike sensible storage, which requires the maintenance of specific temperatures, adsorption-based systems operate based on the principles of adsorption and desorption reactions, eliminating the need for temperature control of the storage material.

While the principle of adsorption-based thermochemical energy storage appears promising, significant advancements are required, particularly concerning the energy storage reactor. This reactor plays a crucial role in facilitating the interaction between flowing air and thermochemical materials, which is pivotal for the effective operation of the system.

1.2. Review of Recent Thermochemical Reactor Developments for Medium- and Low-Temperature Heating

Adsorption-based thermochemical energy storage systems for medium- and low-temperature heating primarily revolve around solid-gas reactive adsorbent–adsorbate working pairs, encompassing pure salt hydrates, porous matrices, and composites composed of salt hydrates and porous matrices [4,5]. Within this context, zeolites, which are renowned for their porous nature, are frequently employed as matrices due to their rapid adsorption capabilities, favorable reaction kinetics, low cost, and high thermal stability [6,7].

In addition to the materials, a surge of thermochemical reactor studies has been conducted with the aim of improving reactor energy storage performance in either charging or discharging processes. Existing thermochemical reactor designs can be classified as stacking [8–10], packing [11–13], modularity [14–16], or heat exchanger modification [17–19] schemes. In order to achieve a satisfactory performance, the targets of reactor studies are (1) an increased contact area between reactants (usually represented by air and a solid thermochemical material) achieved through perforated duct or heat exchanger modifications; (2) a promising theoretical energy storage density achieved by increasing the mass of thermochemical material through stacking and packing configurations, in addition to trials of new materials; and (3) flexible charging and discharging controls achieved by a modularity configuration to allow for charging and discharging control groups.

With respect to the modularity and stacking configurations, Tatsidjodoung et al. [15] tested the thermal performance of a zeolite-based open reactor and achieved an average temperature lift of 38 °C for 40 kg of zeolites during an 8-hour discharging process under an inlet air temperature of 20 °C, specific inlet air humidity of 10 g/kg, and an air flow rate of 180 m³/h. Johannes et al. [20] designed an energy-dense zeolite thermochemical reactor using two storage units, and the obtained thermal efficiency ranged from 34% to 55.1%. Alebeek et al. [16] studied the characteristics of an open, fully packed zeolite/water adsorption heat storage system consisting of four separate segments with 62.5 L of zeolite each, and the maximum output thermal power was 4.4 kW, with a maximum temperature step of 24 °C achieved during the tests. Modularity and stacking can contribute to an energy-dense reactor and flexibility in controlling the charging or discharging sequence. However, there is a list of challenges to be addressed, including slow local diffusion of water molecules, poor air flow uniformity due to the distribution of zeolite particles, increased air resistance, and increased air pressure drop.

On the other hand, other researchers have been working on variations of reactor packing methods to enhance the reaction kinetic performance and airflow uniformity. For example, Zhang et al. [11] investigated the thermal performance of a zeolite 13X-based net-packed thermochemical reactor. The results indicated that a maximum air temperature lift of 38.6 °C was achieved by the copper mesh method, and an energy storage density of 784.4 kJ/kg, along with a thermal efficiency of 38.2%, was also obtained. In addition, the pressure drop was reduced by 28.1% compared with the non-packed method. Ji et al. [12] introduced a multiple-metal mesh-packed method to enhance reactor performance. The cube-shaped mesh configuration achieved an energy storage density of 712.2 kJ/kg and a thermal efficiency of 26.8%. While the packing method demonstrated commendable thermal performance across the entirety of the reactor, the occurrence of non-reaction zones within the particles and inadequate heat–mass transfer rates across each mesh net diminished both the energy storage density and thermal efficiency, which are crucial for energy storage.

1.3. Innovations and Contributions of This Study

While previous studies have made significant strides in improving reactor performance through the use of various reactor configurations and materials, it is necessary to evaluate and identify novel reactor configurations with a balance in terms of reactant–air contact, high theoretical energy density, and flexible charging/discharging control capability. Very few researchers have proposed relevant studies, and additional in-depth work is needed. The authors of [21] proposed a triangular honeycomb zeolite reactor that they compared with a conventional particle-based reactor; the proposed reactor achieved a pressure drop of 235 Pa/m and a 21.93% increase in thermal efficiency. However, the reactor design itself has not been studied in depth, and a list of questions remains to be answered, including with respect to the variations of configurations and the corresponding thermal efficiency under various operating conditions. Therefore, this study presents the following two significant innovations:

(1) In-depth investigations of an innovative triangular honeycomb reactor;
(2) Extensive parametric analysis based on reactor configuration studies.

The data presented in this study can provide significant contributions to thermal energy storage studies and applications, listed as follows.

(1) In-depth studies on a novel triangular honeycomb reactor, with a 140% improvement in air–reactant contact area compared to conventional designs, enhancing energy storage and efficiency;
(2) A detailed critical parametric performance study, including comprehensive analysis of reactor parameters, including energy density, pressure drop, air distribution, and round-trip efficiency, providing new insights into optimal reactor configurations for thermochemical energy storage;
(3) Optimized energy control, offering valuable data to improve flexible charging and discharging controls, ensuring effective energy storage and release;
(4) Contribution to low-carbon heating, including the evaluation of the reactor's feasibility for residential heating applications in cold regions and calculation of the required reactor volume for real-world heating demands.

2. The Energy Storage Process and Descriptions of the Novel Honeycomb Reactor

2.1. Thermochemical Energy Storage Process

The entire thermochemical energy storage system comprises both charging and discharging processes, as illustrated in Figure 1. During the charging phase, ambient air first undergoes preheating in a heat exchanger before passing through an energy source, such as an electric heater powered by off-peak electricity or solar energy, to produce high-temperature hot air. This heated air then travels through the thermochemical reactor, where it causes water molecules to desorb from the honeycomb storage materials, effectively storing heat energy within the thermochemical substances. The energy storage duration can be days or months, as long as the thermochemical material remains separate from the moisture source. Conversely, during the discharging phase, ambient air is humidified using

a moisture source like a humidifier to provide moisture for the energy release reaction. This humidified air is then directed into the honeycomb reactor, where the materials adsorb water molecules from the air, subsequently releasing the stored heat energy. This liberated heat energy is readily available for residential building space-heating applications.
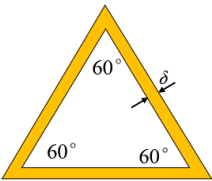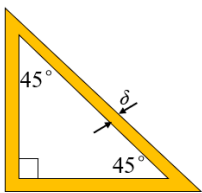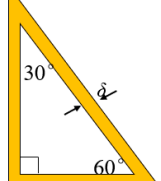

(**a**)

(**b**)
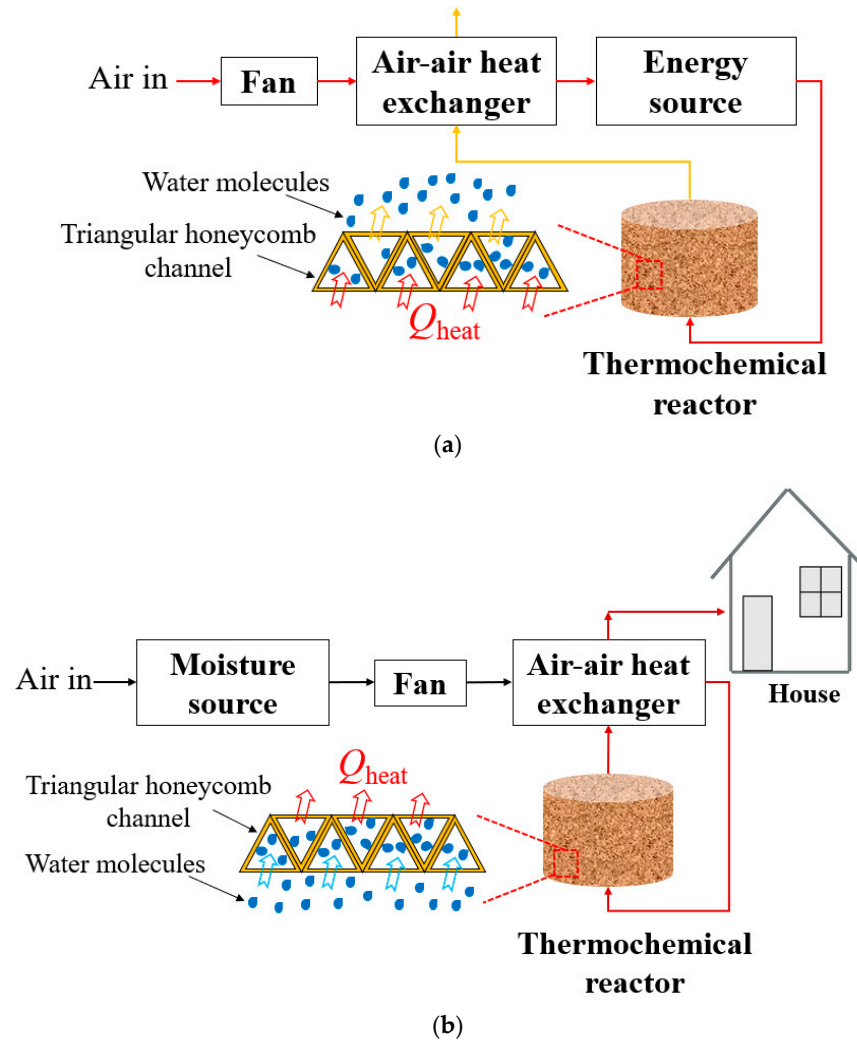
Figure 1. Diagram of heat storage and release during the charging and discharging processes. (**a**) Charging process. (**b**) Discharging process.

2.2. Details on the Triangular Honeycomb Reactor

A schematic representation of the triangular honeycomb reactor is detailed in [21]. In short, it comes with a list of innovations. First, its configuration comprising numerous channels significantly enhances heat and mass transfer rates, thereby reducing reaction times due to the large size of the heat–mass exchange area. Compared to a conventional packed-bed thermochemical reactor with 3–5 mm pellets, at the macroscopic level, this honeycomb shows an increase in the air–reactant contact area of about 140% compared to the conventional setting. Secondly, the increased air–reactant contact helps to reduce the non-reactive zones within the reactor, which effectively boosts achievable energy storage density and thermal efficiency. Additionally, the reduction of pressure loss in the reactor results in decreased electrical consumption by the fan, thereby enhancing overall system efficiency.

A list of structural variations can be applied to the triangular honeycomb reactor. With the aim of increasing the theoretical energy density under a constant reactor volume, three different triangular honeycomb structures are proposed in Table 1.

Table 1. Details of the three different triangular honeycomb channels proposed for space heating.

	Equilateral triangular Side length: e	Right triangle Diagonal side length: e	Right triangle Diagonal side length: e
Triangular honeycomb structure	60°, 60°, 60°, δ	45°, 45°, δ	30°, 60°, δ
Side length (mm)	2.13, 2.13, 2.13	$\frac{2.13}{\sqrt{2}}$, $\frac{2.13}{\sqrt{2}}$, 2.13	$\frac{2.13}{2}$, $\frac{2.13\sqrt{3}}{2}$, 2.13
Single-channel thickness (mm)	0.265	0.265	0.265
Channel length (mm)	100	100	100
Perimeter of inner channel (mm)	$3 \times 2.13 = 6.39$	$2.13 + 2.13\sqrt{2} \approx 5.14$	$2.13 + \frac{2.13(1+\sqrt{3})}{2} \approx 5.04$
Zeolite mass ($kg_{zeolite}$)	3.38	4.03	4.26
Channel number	48,808	67,560	70,839
Reactor volume (m^3)	0.0196	0.0196	0.0196

3. Numerical Model Establishment

3.1. Numerical Model Description

The triangular honeycomb reactor, composed of multiple channels, assumes uniform heat and mass transfer performance, so a single channel is selected as the calculation domain. A single triangular honeycomb channel with a length of L is chosen as the computation domain, as shown in Figure 2.

(a)

(b)
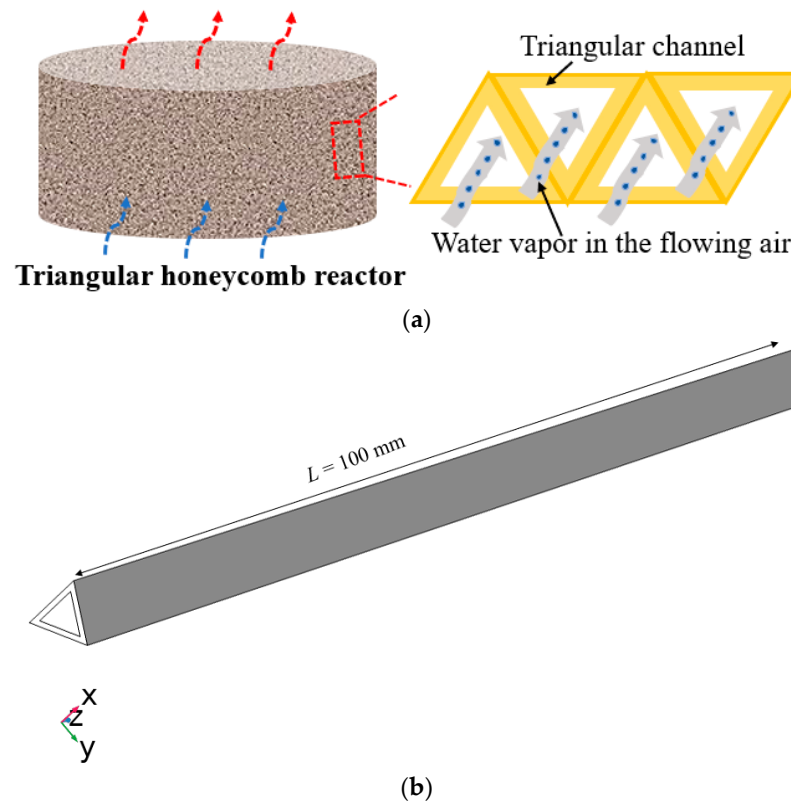
Figure 2. Geometric model of the triangular honeycomb channels and a simulated 3D illustration. (**a**) Schematic diagram of the triangular honeycomb reactor during the discharging process. (**b**) 3D schematic of the single triangular honeycomb channel used in the computation model.

The triangular honeycomb reactor consists of multiple small honeycomb channels, and for the purposes of numerical analysis, the following assumptions are made:

- All triangular honeycomb channels are assumed to have the same heat and mass transfer performance. This assumption simplifies the calculation of the reactor's thermal performance by treating each channel equivalently [22].
- The fluid inside the air channel is regarded as an ideal gas. This assumption is widely used in thermochemical modeling to streamline analysis, especially when dealing with air flow at moderate temperatures and pressures [23].
- Heat conduction and mass diffusion are considered within the triangular honeycomb channels, with the thermal conductivity, specific heat, and density of both air and zeolite 13X taken as functions of water vapor content. This enables the model to account for heat and mass transport processes during adsorption and desorption [24].
- It is assumed that the adsorption/desorption heat is sufficiently absorbed or diffused by the reactant layer, allowing for efficient energy storage and release within the reactor [25].
- Radiative heat transfer inside the reactor is considered negligible. This assumption is made to simplify the model, as the impact of radiation is minimal compared to convection and conduction at the temperature levels being studied.

These assumptions are made to focus on macroscopic phenomena, measuring performance at the scale of meters or millimeters rather than at the molecular level. The key benefits of these assumptions include reducing computational complexity, increasing computational efficiency, and decreasing overall simulation time. However, a drawback is that the model does not fully replicate the microscopic interactions or the detailed molecular dynamics that occur within each channel.

3.2. Descriptions of Heat and Mass Transfer

3.2.1. Heat Transfer and Energy Balance

Equations (1) and (2) depict heat transfer in flowing air and thermochemical material.

$$\rho_{\text{ha}} c_{\text{p,ha}} \frac{\partial T}{\partial t} + \rho_{\text{ha}} c_{\text{p,ha}} v \nabla T + \nabla \cdot (-k_{\text{ha}} \nabla T) = 0 \tag{1}$$

$$\rho_{\text{tot}} c_{\text{p,tot}} \frac{\partial T}{\partial t} = \nabla \cdot (k_{\text{tot}} \nabla T) + M_{\text{w}} \left((1 - \varepsilon) \frac{\partial C_z}{\partial t} - \nabla \cdot (D_{\text{s,eff}} \nabla C_z) \right) \cdot \Delta H \tag{2}$$

Here, ρ_{ha} is the humid air density (kg/m^3), $c_{\text{p,ha}}$ is the specific heat of humid air (J/(kg·K)), and k_{ha} is the thermal conductivity of humid air (W/(m·K)). ρ_{tot} is the density of the entire adsorbent layer (kg/m^3), including adsorbed water and porous adsorbents; $c_{\text{p,tot}}$ is the specific heat of adsorbent layer (J/(kg·K)); and k_{tot} is the thermal conductivity of the adsorbent layer (W/(m·K))—all of which are functions of water vapor, as shown in Table 2. v is velocity (m/s), M_{w} is the molar mass of the water vapor (kg/mol), $D_{\text{s,eff}}$ is the effective surface diffusivity (m^2/s), C_z is the water concentration in the matrix of zeolites (mol/m^3), ε is the porosity of zeolites, and ΔH is the heat of adsorption (J/kg).

The heat of adsorption $(\Delta H (\text{J/kg}))$ is related to the water uptake (w) of zeolite 13X [26], which can be calculated by Equation (3).

$$\Delta H = \left(7 \times 10^7 w^6 - 7 \times 10^7 w^5 + 3 \times 10^7 w^4 - 7 \times 10^6 w^3 + 89{,}9951 w^2 - 69{,}983 w + 6491.3 \right) \times 1000 \tag{3}$$

3.2.2. Mass Transfer and Mass Balance

Moisture in flowing air during the discharging process is adsorbed by the thermochemical material, which includes dry air and water vapor. The moisture is also adsorbed by the zeolites, then diffuses into the pores and matrix of the zeolite 13X [23]. Therefore, the moisture diffused in the air and zeolite 13X can be depicted by Equations (4) and (5), respectively.

$$\frac{\partial C_{\mathrm{a}}}{\partial t} + v\nabla C_{\mathrm{a}} + \nabla\cdot(-D_{\mathrm{v,a}}\nabla C_{\mathrm{a}}) = 0 \tag{4}$$

$$\varepsilon\frac{\partial C_{\mathrm{p}}}{\partial t} + (1-\varepsilon)\frac{\partial C_{\mathrm{z}}}{\partial t} = \nabla\cdot\left(D_{\mathrm{p,eff}}\nabla C_{\mathrm{p}}\right) + \nabla\cdot(D_{\mathrm{s,eff}}\nabla C_{\mathrm{z}}) \tag{5}$$

Here, C_{a} is the water concentration within the air $(\mathrm{mol/m^3})$, $D_{\mathrm{v,a}}$ is the molecular diffusivity of water in air $(\mathrm{m^2/s})$, C_{p} is the concentration of water in the adsorbent pores $(\mathrm{mol/m^3})$, and $D_{\mathrm{p,eff}}$ is the effective pore diffusivity $(\mathrm{m^2/s})$ inside the porous zeolite.

The initial thermo-physical parameters of air, water vapor, liquid water, and zeolite 13X, along with other calculation parameters required for the whole reaction process, are presented in Table 2 and Ref. [21].

Table 2. Thermo-physical parameters of humid air and humid zeolite 13X.

Air	$\rho_{\mathrm{ha}} = \rho_{\mathrm{a}}(1+w_1)$ $w_1 = \frac{C_{\mathrm{a}}RT_{\mathrm{a}}M_{\mathrm{w}}}{P_0 M_{\mathrm{a}} - C_{\mathrm{a}}RT_{\mathrm{a}}M_{\mathrm{a}}}$ $c_{\mathrm{p,ha}} = \frac{\rho_{\mathrm{a}}c_{\mathrm{p,a}} + w_1\rho_{\mathrm{a}}c_{\mathrm{p,v}}}{\rho_{\mathrm{ha}}}$ $k_{\mathrm{ha}} = \frac{\rho_{\mathrm{a}}k_{\mathrm{a}} + w_1\rho_{\mathrm{a}}k_{\mathrm{v}}}{\rho_{\mathrm{ha}}}$
Zeolite 13X	$\rho_{\mathrm{tot}} = \varepsilon\rho_{\mathrm{zp}} + (1-\varepsilon)\rho_{\mathrm{zm}}$ $\rho_{\mathrm{zp}} = \rho_{\mathrm{a}}(1+w_2)$ $\rho_{\mathrm{zm}} = \rho_{\mathrm{z}}(1+w)$ $w_2 = \frac{C_{\mathrm{p}}RT_{\mathrm{a}}M_{\mathrm{w}}}{P_0 M_{\mathrm{a}} - C_{\mathrm{p}}RT_{\mathrm{a}}M_{\mathrm{a}}}$ $w = \frac{C_{\mathrm{z}}M_{\mathrm{w}}}{\rho_{\mathrm{z}}}$ $c_{\mathrm{p,zp}} = \frac{\rho_{\mathrm{a}}c_{\mathrm{p,a}} + w_2\rho_{\mathrm{a}}c_{\mathrm{p,v}}}{\rho_{\mathrm{zp}}}$ $c_{\mathrm{p,zm}} = \frac{\rho_{\mathrm{z}}c_{\mathrm{p,z}} + w\rho_{\mathrm{z}}c_{\mathrm{p,l}}}{\rho_{\mathrm{zm}}}$ $c_{\mathrm{p,tot}} = \frac{(1-\varepsilon)\rho_{\mathrm{zm}}c_{\mathrm{p,zm}} + \varepsilon\rho_{\mathrm{zp}}c_{\mathrm{p,zp}}}{\rho_{\mathrm{tot}}}$ $k_{\mathrm{zm}} = \frac{\rho_{\mathrm{z}}k_{\mathrm{z}} + w\rho_{\mathrm{z}}k_{\mathrm{l}}}{\rho_{\mathrm{zm}}}$ $k_{\mathrm{zp}} = \frac{\rho_{\mathrm{a}}k_{\mathrm{a}} + w_2\rho_{\mathrm{a}}k_{\mathrm{v}}}{\rho_{\mathrm{zp}}}$ $k_{\mathrm{tot}} = \frac{(1-\varepsilon)\rho_{\mathrm{zm}}k_{\mathrm{zm}} + \varepsilon\rho_{\mathrm{zp}}k_{\mathrm{zp}}}{\rho_{\mathrm{tot}}}$

3.2.3. Adsorption Kinetics

A Linear Driving Force (LDF) model to describe diffusion-controlled kinetics was proposed by Glueckauf [27], as depicted by Equation (6).

$$\frac{\partial w}{\partial t} = k_{\mathrm{LDF}}(w_{\mathrm{eq}} - w) \tag{6}$$

where $\frac{\partial w}{\partial t}$ denotes the adsorption reaction rate $(\mathrm{kg/(kg\cdot s)})$ and w_{eq} is the equilibrium water concentration $(\mathrm{kg_{water}/kg_{zeolite}})$. The effective rate coefficient $(k_{\mathrm{LDF}}\ (1/\mathrm{s}))$ is calculated by Glueckauf approximation [28] and based on the properties of zeolites [29].

The equilibrium adsorption of water vapor in zeolite 13X is expressed by an adsorption curve [30,31]. The maximum amount of moisture that zeolite 13X can adsorb is a function of relative humidity $(\varnothing_{\mathrm{z}})$, which can be calculated using Equation (7).

$$w_{\mathrm{eq}} = \left(185.2\frac{14.87\varnothing_{\mathrm{z}}}{1+14.87\varnothing_{\mathrm{z}}} + 9.067\varnothing_{\mathrm{z}} + 3.608\frac{\varnothing_{\mathrm{z}}}{1-\varnothing_{\mathrm{z}}}\right)/\rho_{\mathrm{z}} \tag{7}$$

where w_{eq} is the equilibrium among of moisture adsorption by the adsorbent $(\mathrm{kg/kg})$ and $\varnothing_{\mathrm{z}}$ is the relative humidity of zeolite (%).

3.2.4. Initial and Boundary Conditions

The initial state and boundary conditions for the charging and discharging processes in the modeling simulation are shown in Table 3.

Table 3. Initial and boundary conditions for charging and discharging processes.

	Initial Conditions	Inlet Air Conditions
Charging	$\varnothing_{z,ini} = 90\%, 93\%, 95\%, 97\%$ $T_{amb} = 25\,^{\circ}C$ $T_{z,ini} = 25\,^{\circ}C$	$\dot{m}_{char,in} = 129\ kg/h$ $\varnothing_{char,in} = 0$ $T_{char,in} = 25–180\,^{\circ}C$
Discharging	$\varnothing_{z,ini} = 10\%, 7\%, 5\%, 3\%$ $T_{amb} = 25\,^{\circ}C$ $T_{z,ini} = 25\,^{\circ}C$	$\dot{m}_{dis,in} = 46\ kg/h$ $\varnothing_{dis,in} = 70\%, 98\%$ $T_{dis,in} = 25\,^{\circ}C$
Outlet air conditions [22]		
Outlet atmospheric air pressure		$\left[-PI + \mu \left(\nabla u + (\nabla u)^T \right) \right] n = -\hat{P}_0 n$
All variables have zero normal gradients at the outlet.		$-n \cdot D_{v,a} \nabla C_a = 0$ $-n \cdot (-k_{ha} \nabla T) = 0$
Interface boundary conditions [22]		
Boundary conditions at the air–adsorbent interface layer are derived from mass and energy balances as follows:		
	$-\rho_a D_{p,eff} \frac{\partial C_p}{\partial n} - \rho_z D_{s,eff} \frac{\partial C_z}{\partial n} = -\rho_a D_{v,a} \frac{\partial C_a}{\partial n}$ $-k_{tot} \frac{\partial T}{\partial n} = -k_{ha} \frac{\partial T}{\partial n} - M_w D_{s,eff} \frac{\partial C_z}{\partial n} \Delta H$	
Wall boundary conditions		
There is no heat flux for the adsorbent layer.		

3.3. Performance Indicators of the Proposed Thermochemical Reactor

In the adsorption heat storage system, energy storage density and thermal efficiency are key indicators for the assessment of the system's feasibility [11], as depicted in the Table 4. The energy storage density reflects the ratio of thermal energy cumulated during the discharging process to the mass of zeolites, while thermal efficiency is the ratio of cumulative thermal energy for the discharging process to the cumulative thermal energy for the charging process. During the charging process, instantaneous heat transfer to the adsorbents and the thermal energy cumulated over the charging reaction time are represented by Equations (8) and (9), respectively. The instantaneous heat released from the adsorbents and the thermal energy cumulated during the discharging reaction time are described by Equations (10) and (11), respectively. The energy storage density and thermal efficiency are determined by the thermal energy cumulated during the charging and discharging processes, as shown in Equations (12) and (13).

Table 4. Equations of reactor performance during the charging and discharging processes.

	Description	Unit	Equation	
Charging	Instantaneous heat transfer to adsorbents	W	$\dot{Q}_{char,tr} = \dot{h}_{char,in} - \dot{h}_{char,out}$	(8)
	Cumulation of thermal energy by adsorbents	J	$Q_{char,cum} = \int_0^{t_{char}} \left(\dot{h}_{char,in} - \dot{h}_{char,out} \right) dt$	(9)
Discharging	Instantaneous heat release from adsorbents	W	$\dot{Q}_{dis,re} = \dot{h}_{dis,out} - \dot{h}_{dis,in}$	(10)
	Release of cumulated thermal energy by adsorbents	J	$Q_{dis,cum} = \int_0^{t_{dis}} \left(\dot{h}_{dis,out} - \dot{h}_{dis,in} \right) dt$	(11)
Energy storage density		J/kg	$ESD = \frac{Q_{dis,cum}}{m_{zeolite}}$	(12)
Reactor thermal efficiency		%	$\eta = \frac{Q_{dis,cum}}{Q_{char,cum}} \times 100\%$	(13)

The specific enthalpy of humid air is calculated using Equation (14), while the absolute humidity of air (w_1) is determined by Equations (15) and (16) [21].

$$h = c_{p,a} \cdot (T_a - 273) + w_1 \cdot (2501 + c_{p,v} \cdot (T_a - 273)) \tag{14}$$

$$w_1 = \frac{0.622 \phi P_{sat}}{P_0 - \phi P_{sat}} \tag{15}$$

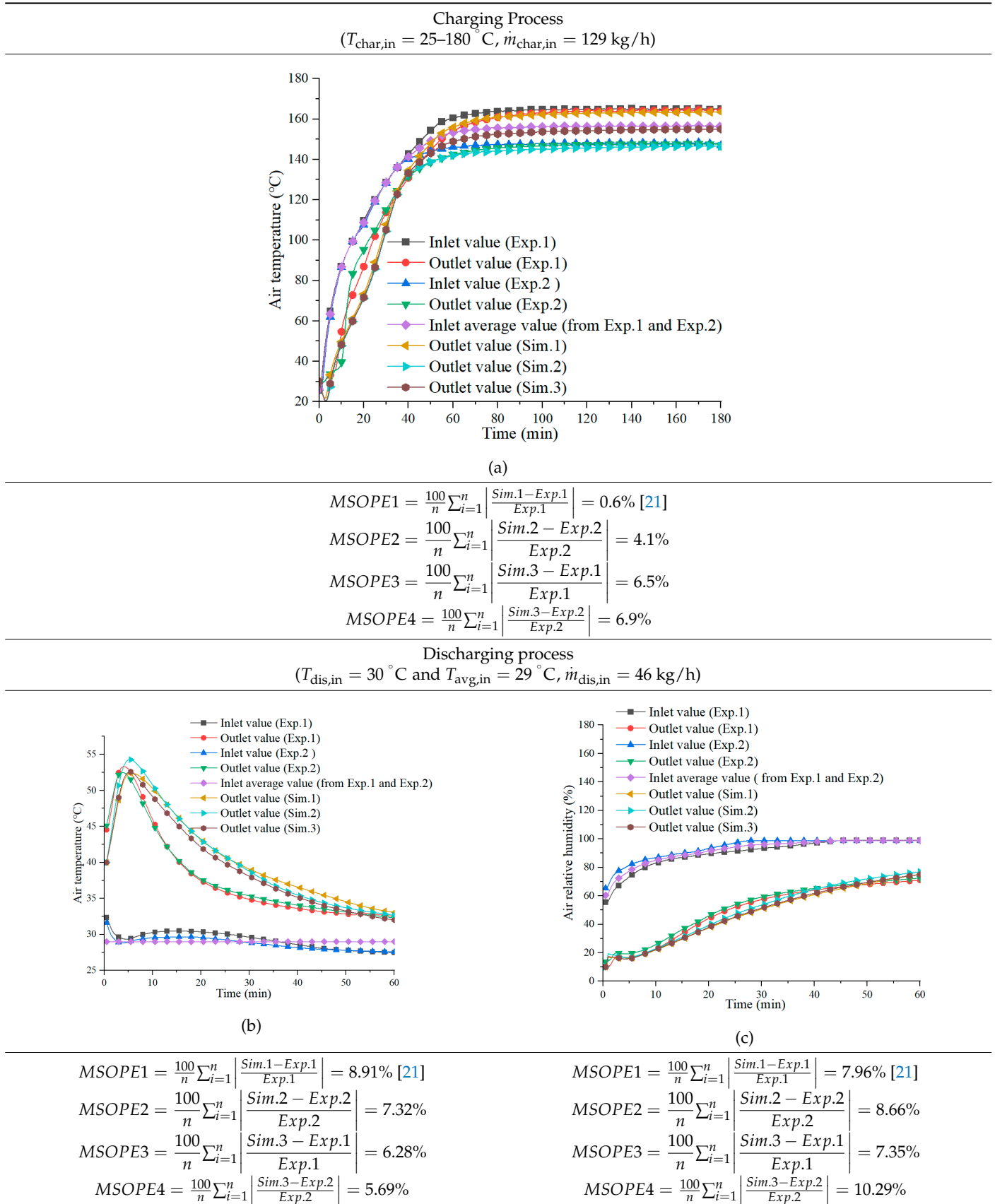$$P_{sat} = \exp\left(23.196 - \frac{3816.44}{T_a - 46.13}\right) \tag{16}$$

3.4. Model Validations

The equations were solved using COMSOL Multiphysics, employing the finite difference method with a time step of 30 s. This approach ensured accurate and stable simulations of the heat and mass transfer processes within the triangular honeycomb reactor. The numerical model shows an accurate representation of both reactor charging and discharging process with data on air temperature and humidity.

Table 5 depicts the mean sum of the percent error (MSOPE) between experimental tests and simulation results during the charging and discharging processes. Two sets of experimental tests were conducted under the same settings for charging and discharging processes to obtain sufficient test data on the changes in air temperature and the relative humidity of air. Details of the experimental setup can be found in [32]. According to analysis of the results of experimental tests and simulation, the MSOPE matches well between experimental data and simulation data. Due to the slight differences in air temperature and air relative humidity during the experimental test due to effects of the external environment, like weather, the experimental data present a minor variation in the input data (for instance, the inlet air temperature during discharging), leading to MSOPE variations.

In our previously published work [21], which involved another experimental test, the mean sum of deviations in percentage errors between simulation results and experimental tests for outlet air temperature were 0.6% and 4.1%, respectively, during the charging process. The mean sum of deviations in percentage error between simulation results and experimental tests for outlet air temperature and the outlet relative humidity of air during the discharging process (using discharging test data from Exp. 2 reported in [32]) were 8.91% and 7.32% for temperature and 7.96% and 8.66% for relative humidity, respectively. Using the average values of the inlet air temperature and inlet relative humidity of air during the charging and discharging processes, simulation 3 was conducted to investigate the influence of average inlet air temperature and the average inlet relative humidity of air during the two experimental tests of the heat and mass transfer model. For the charging process, the average inlet air temperature improved MSOPE values between Exp.1 and Sim.3 and between Exp.2 and Sim.3. The average inlet air temperature of 29 °C obviously decreased the deviations between Exp.1 and Sim.3 and between Exp.2 and Sim.3. Additionally, the average inlet relative humidity of air in Exp.1 and Exp.2 slightly reduced the MSOPE value between Exp.1 and Sim.3. However, the average inlet relative humidity of air in Exp.1 and Exp.2 resulted in the highest MSOPE value of 10.29% between Exp.2 and Sim.3. According to the literature, an average deviation of less than 12% can yield an accurate modeling result [13,33–35]. Therefore, the proposed heat and mass transfer model is validated and can accurately predict the heat and mass transfer performance between flowing air and triangular honeycomb channels. The validated model was used to investigate and analyze the heat and mass transfer performance of three different triangular reactors in this study.

Table 5. Analysis of the mean sum of the percentage errors between experimental tests and simulation results during the charging and discharging processes.
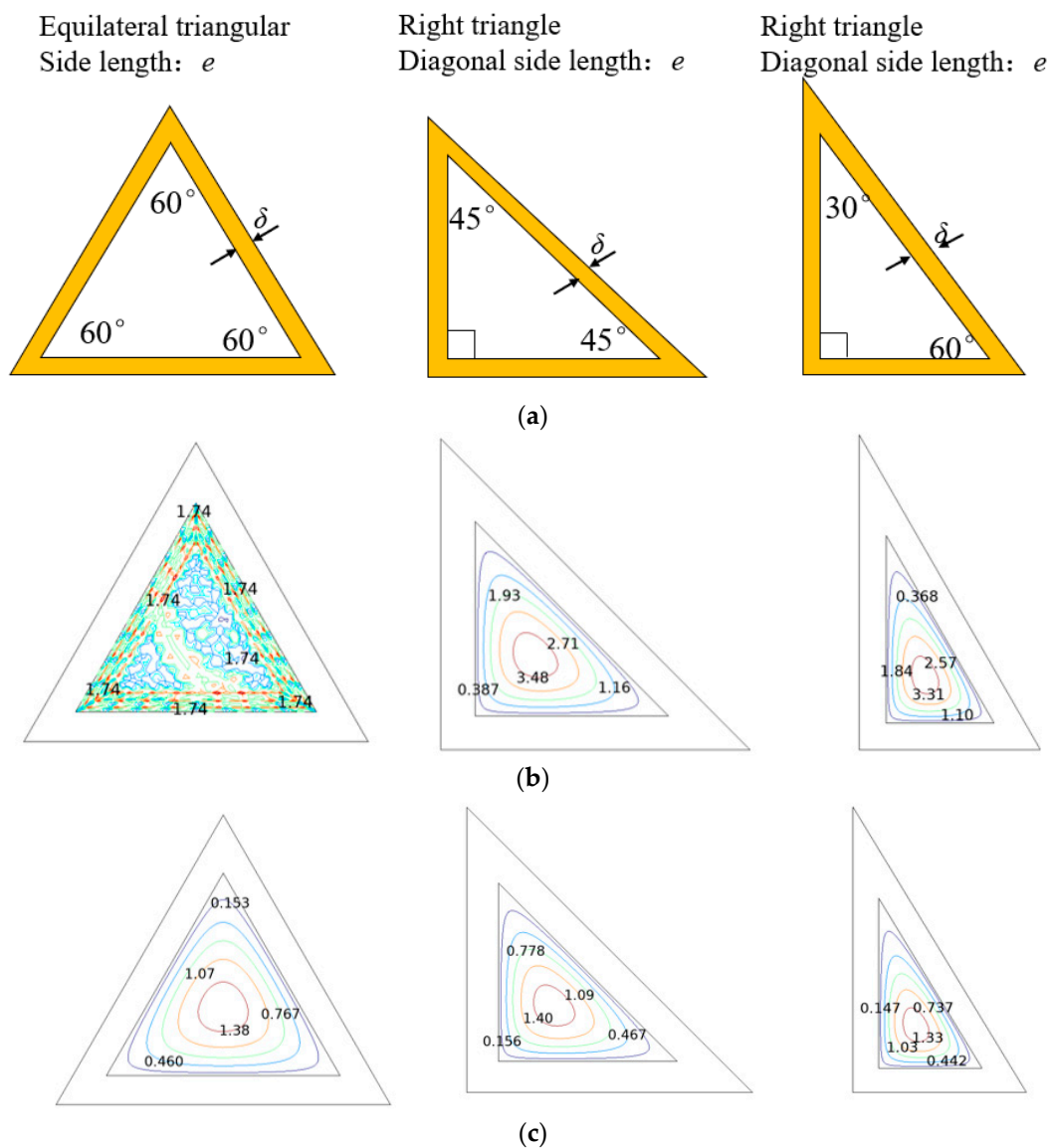
Charging Process
($T_{\text{char,in}} = 25\text{–}180\ ^{\circ}\text{C}$, $\dot{m}_{\text{char,in}} = 129\ \text{kg/h}$)

(a)

$$MSOPE1 = \frac{100}{n}\sum_{i=1}^{n}\left|\frac{Sim.1 - Exp.1}{Exp.1}\right| = 0.6\%\ [21]$$

$$MSOPE2 = \frac{100}{n}\sum_{i=1}^{n}\left|\frac{Sim.2 - Exp.2}{Exp.2}\right| = 4.1\%$$

$$MSOPE3 = \frac{100}{n}\sum_{i=1}^{n}\left|\frac{Sim.3 - Exp.1}{Exp.1}\right| = 6.5\%$$

$$MSOPE4 = \frac{100}{n}\sum_{i=1}^{n}\left|\frac{Sim.3 - Exp.2}{Exp.2}\right| = 6.9\%$$

Discharging process
($T_{\text{dis,in}} = 30\ ^{\circ}\text{C}$ and $T_{\text{avg,in}} = 29\ ^{\circ}\text{C}$, $\dot{m}_{\text{dis,in}} = 46\ \text{kg/h}$)

(b)

(c)

$$MSOPE1 = \frac{100}{n}\sum_{i=1}^{n}\left|\frac{Sim.1 - Exp.1}{Exp.1}\right| = 8.91\%\ [21]$$

$$MSOPE2 = \frac{100}{n}\sum_{i=1}^{n}\left|\frac{Sim.2 - Exp.2}{Exp.2}\right| = 7.32\%$$

$$MSOPE3 = \frac{100}{n}\sum_{i=1}^{n}\left|\frac{Sim.3 - Exp.1}{Exp.1}\right| = 6.28\%$$

$$MSOPE4 = \frac{100}{n}\sum_{i=1}^{n}\left|\frac{Sim.3 - Exp.2}{Exp.2}\right| = 5.69\%$$

$$MSOPE1 = \frac{100}{n}\sum_{i=1}^{n}\left|\frac{Sim.1 - Exp.1}{Exp.1}\right| = 7.96\%\ [21]$$

$$MSOPE2 = \frac{100}{n}\sum_{i=1}^{n}\left|\frac{Sim.2 - Exp.2}{Exp.2}\right| = 8.66\%$$

$$MSOPE3 = \frac{100}{n}\sum_{i=1}^{n}\left|\frac{Sim.3 - Exp.1}{Exp.1}\right| = 7.35\%$$

$$MSOPE4 = \frac{100}{n}\sum_{i=1}^{n}\left|\frac{Sim.3 - Exp.2}{Exp.2}\right| = 10.29\%$$

Notes: charging test data and discharging test data for Exp.1 and Exp.2 from literatures [21] and [32], respectively.

4. Results and Evaluations of the Proposed Reactor Configurations

4.1. Air Velocity Distribution

Figure 3 illustrates the distribution of air velocity within a single triangular honeycomb channel under identical air velocity conditions. During the charging phase, the triangular honeycomb channel with angles of 60°, 60°, and 60° exhibits a more uniform air velocity distribution than the other two triangular honeycomb channels. This variation is attributed to differences in honeycomb shape and the hydraulic diameter of the channels. Additionally, the triangular honeycomb channel with angles of 45°, 45°, and 90° displays slightly higher air velocity distribution than the channel with angles of 30°, 60°, and 90°. Specifically, the maximum air velocity reaches 3.48 m/s and 1.40 m/s at the center of the triangular honeycomb channel during the charging and discharging processes, respectively.

Figure 3. Air velocity distribution in a triangular honeycomb. (**a**) Triangular shapes. (**b**) Air distribution during the charging process. (**c**) Air distribution during the discharging process.

4.2. Air Temperature during the Charging Process

The outlet air temperature value for three different triangular honeycomb reactors with the same initial relative humidity of zeolites during the charging process basically has the same increasing trend, as shown in Figure 4. A higher initial relative humidity of zeolites results in higher absolute outlet air humidity; the highest absolute outlet air

humidity is up to 0.019 kg/kg for the triangular honeycomb reactor with angles of 30°, 60°, and 90° under an initial relative humidity of 97%. This is attributed to the increased adsorption of water molecules by zeolite during the discharging process, leading to higher initial relative humidity and subsequently elevated absolute outlet air humidity during the charging phase. Additionally, due to the different triangular honeycomb shapes and air velocity distributions in the channel, the triangular honeycomb reactor with angles of 60°, 60°, and 60° presents the lowest absolute outlet air humidity under the same initial conditions, and the triangular honeycomb reactor with angles of 30°, 60°, and 90° exhibits the highest absolute outlet air humidity among three triangular honeycomb reactors.
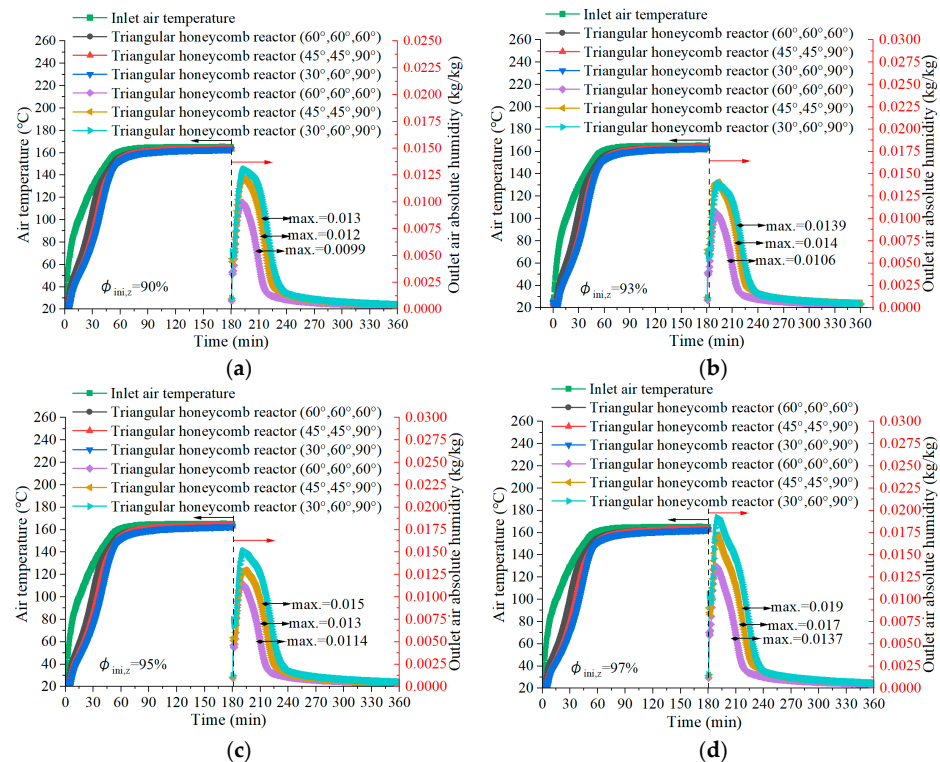
Figure 4. Air temperature and absolute outlet air humidity changes among three different triangular honeycomb reactors during the charging process. At (**a**) $\varnothing_{ini,z} = 90\%$, (**b**) $\varnothing_{ini,z} = 93\%$, (**c**) $\varnothing_{ini,z} = 95\%$ and (**d**) $\varnothing_{ini,z} = 97\%$.

4.3. Air Temperature Lift in Discharging

Air temperature lift between the outlet air temperature and inlet air temperature during the discharging process is used to evaluate the key parameter of the thermal performance of the reactor. Figure 5 illustrates the impact of the initial relative humidity of zeolites and the relative humidity of inlet air on air temperature lift. A lower initial relative humidity of zeolites results in more heat energy stored inside the reactor, which contributes to a higher air temperature lift. A higher relative humidity of inlet air also helps to increase air temperature lift. The highest air temperature lift among the three different reactors is achieved at 48.7 °C by the triangular honeycomb reactor with angles of 30°, 60°, and 90° under an initial relative humidity of zeolites of 3% and a relative humidity of inlet air of 98%. Compared with the other two triangular honeycomb reactors with angles of 45°, 45°, and 90° and 30°, 60°, and 90°, the triangular honeycomb reactor with angles of 60°, 60°, and 60° presents the lowest air temperature lift and the highest absolute outlet air humidity due to it having the largest heat-exchange area, which accelerates the heat and mass transfer rate between flowing air and zeolite 13X. The triangular honeycomb reactor with angles of 30°, 60°, and 90° achieves the highest air temperature lift and the lowest absolute outlet air humidity under the same initial conditions, including the same relative humidity of inlet air, during the discharging process. It has the lowest air velocity

distribution among the three different triangular honeycomb channels and the smallest heat–mass exchange areas, which slows down the heat and mass transfer rate, leading to an increase in air temperature lift and a decrease in the absolute humidity of outlet air.
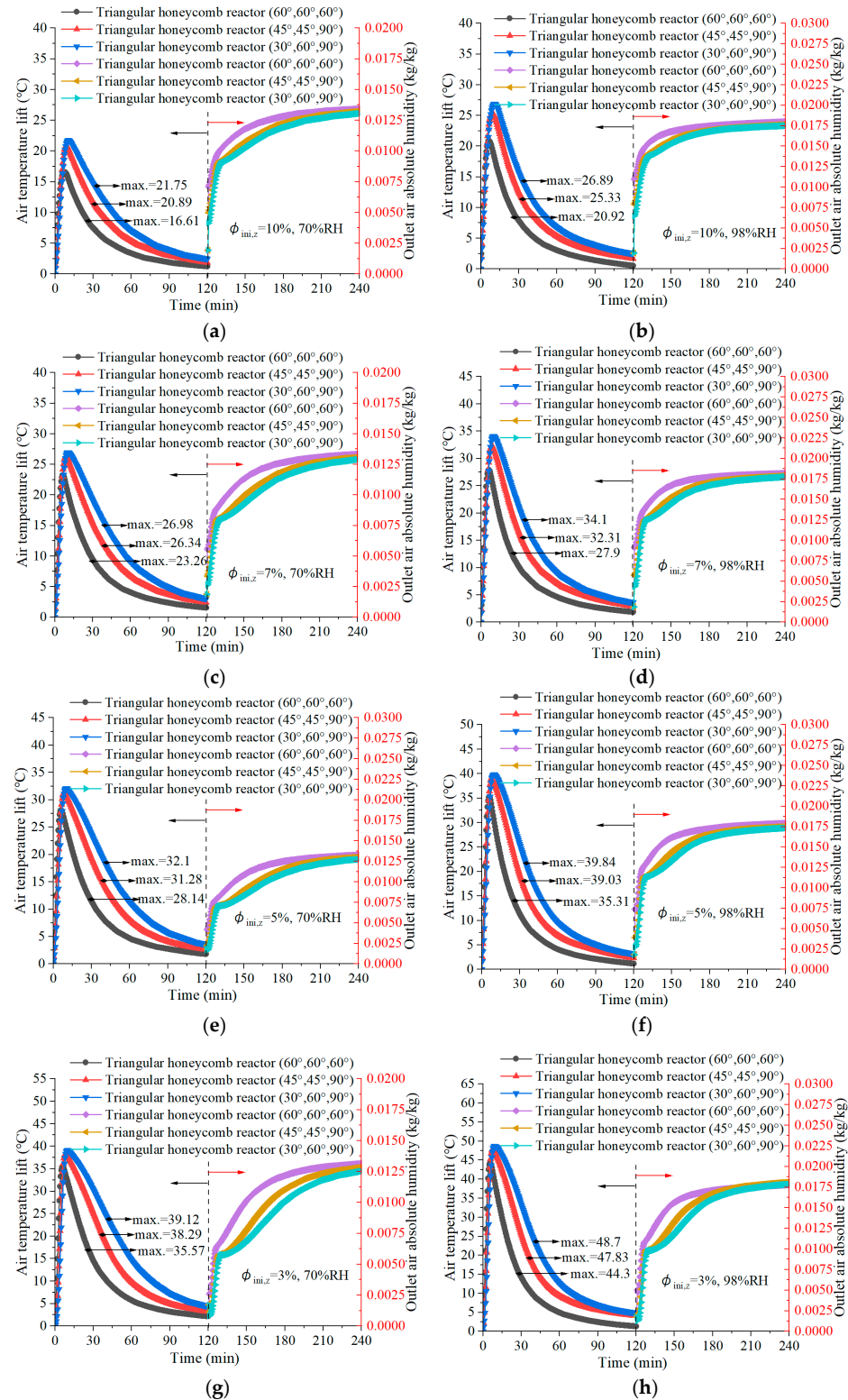
Figure 5. Air temperature lift changes among three different triangular honeycomb reactors during the discharging process. (**a**) $\varnothing_{ini,z} = 10\%$, 70%RH; (**b**) $\varnothing_{ini,z} = 10\%$, 98%RH; (**c**) $\varnothing_{ini,z} = 7\%$, 70%RH; (**d**) $\varnothing_{ini,z} = 7\%$, 98%RH; (**e**) $\varnothing_{ini,z} = 5\%$, 70%RH; (**f**) $\varnothing_{ini,z} = 5\%$, 98%RH; (**g**) $\varnothing_{ini,z} = 3\%$, 70%RH and (**h**) $\varnothing_{ini,z} = 3\%$, 98%RH.

Based on the discussions presented above, Table 6 presents a comparison of the rate of peak air temperature lift of the triangular honeycomb reactor with angles of 60°, 60°, and 60° during the charging and discharging processes. During the charging process, compared with the triangular honeycomb reactor with angles of 60°, 60°, and 60°, the maximum increment rates of air temperature lift are 28.93% for the triangular honeycomb reactor with angles of 45°, 45°, and 90° and 40.86% for the triangular honeycomb reactor with angles of 30°, 60°, and 90° under an initial relative humidity of zeolites of 93% and 97%, respectively. For the discharging process, a lower initial relative humidity of zeolites results in a lower increment rate of air temperature lift. The increment rate of air temperature lift for the triangular honeycomb reactor with angles of 30°, 60°, and 90° is obviously higher than that for the triangular honeycomb reactor with angles of 45°, 45°, and 90°, which results from multiple factors, for example, air velocity distribution, heat–mass exchange area, triangular honeycomb shape, and hydraulic diameter. The maximum increment rates of air temperature lift are 25.77% for the triangular honeycomb reactor with angles of 45°, 45°, and 90° and 30.95% for the triangular honeycomb reactor with angles of 30°, 60°, and 90° under the same conditions of an initial relative humidity of zeolites of 10% and a relative humidity of inlet air of 70%.

Table 6. Increment rate of peak air temperature lift compared with a triangular honeycomb reactor with angles of 60°, 60°, and 60°.

Reactor	Process	Operating Conditions	Increment Rate of Peak Air Temperature Lift Compared with Triangular Honeycomb Reactor with Angles of 60°, 60°, and 60°
Triangular honeycomb reactor with angles of 45°, 45°, and 90°	Charging	$\varnothing_{ini,z} = 90\%$	24.82%
		$\varnothing_{ini,z} = 93\%$	28.93%
		$\varnothing_{ini,z} = 95\%$	20.71%
		$\varnothing_{ini,z} = 97\%$	25.22%
	Discharging	$\varnothing_{ini,z} = 10\%$, RH = 70%	25.77%
		$\varnothing_{ini,z} = 10\%$, RH = 98%	21.08%
		$\varnothing_{ini,z} = 7\%$, RH = 70%	13.24%
		$\varnothing_{ini,z} = 7\%$, RH = 98%	15.81%
		$\varnothing_{ini,z} = 5\%$, RH = 70%	11.16%
		$\varnothing_{ini,z} = 5\%$, RH=98%	10.54%
		$\varnothing_{ini,z} = 3\%$, RH = 70%	7.65%
		$\varnothing_{ini,z} = 3\%$, RH = 98%	7.97%
Triangular honeycomb reactor with angles of 30°, 60°, and 90°	Charging	$\varnothing_{ini,z} = 90\%$	39.32%
		$\varnothing_{ini,z} = 93\%$	39.12%
		$\varnothing_{ini,z} = 95\%$	38.94%
		$\varnothing_{ini,z} = 97\%$	40.86%
	Discharging	$\varnothing_{ini,z} = 10\%$, RH = 70%	30.95%
		$\varnothing_{ini,z} = 10\%$, RH = 98%	28.54%
		$\varnothing_{ini,z} = 7\%$, RH = 70%	15.99%
		$\varnothing_{ini,z} = 7\%$, RH = 98%	22.22%
		$\varnothing_{ini,z} = 5\%$, RH=70%	14.07%
		$\varnothing_{ini,z} = 5\%$, RH = 98%	12.83%
		$\varnothing_{ini,z} = 3\%$, RH = 70%	9.98%
		$\varnothing_{ini,z} = 3\%$, RH = 98%	9.93%

4.4. Pressure Drop during the Discharging Process

Pressure loss is a key parameter for the evaluation of a reactor's thermal performance during the discharging process. Changes in pressure drop are also related to the air flow direction, the dynamic viscosity coefficient of air, the air flow rate, particles size, and the porosity of the reactor [11]. Figure 6 shows a comparative analysis of the three different triangular honeycomb reactors under the same operating conditions. Obviously, the triangular honeycomb reactor with angles of 60°, 60°, and 60° presents the lowest the pressure drop value of 226.12 Pa/m. Compared with the triangular honeycomb reactor with angles of 60°, 60°, and 60°, the pressure drop values for the triangular honeycomb reactor with angles of 45°, 45°, and 90° and the triangular honeycomb reactor with angles of 30°, 60°, and 90° increase by 204.43 Pa/m and 296.77 Pa/m, respectively, with the highest pressure drop improvement rate of 131.24%.
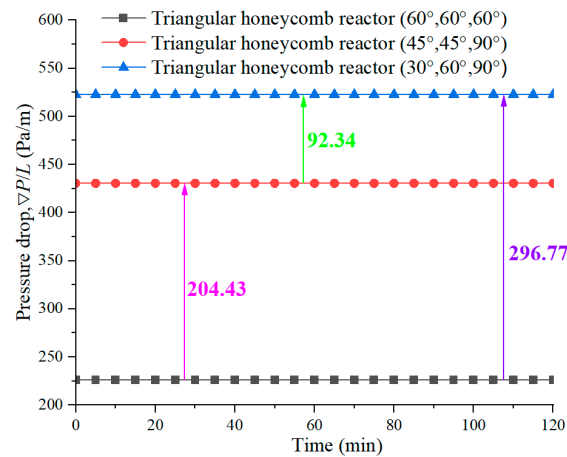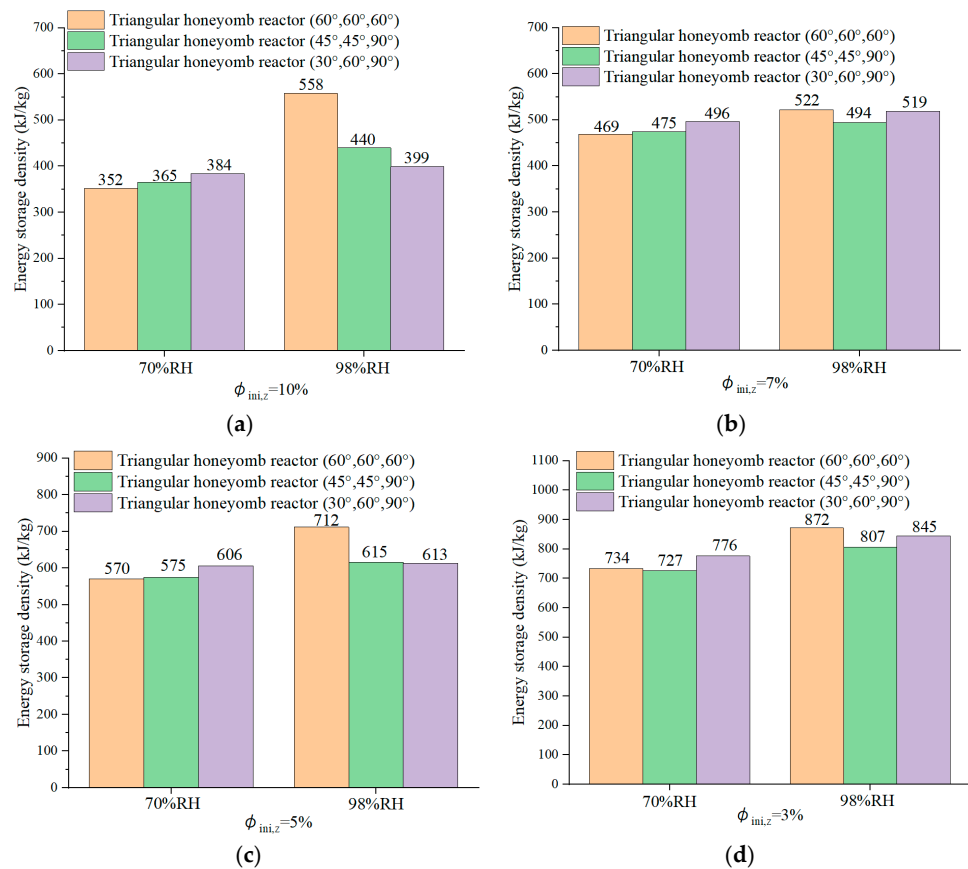
Figure 6. Pressure drop changes for different triangular honeycomb zeolite 13X reactors during the discharging process.

4.5. Energy Storage Density for Triangular Honeycomb Zeolite 13X Reactors

Figure 7 illustrates the effects of the initial relative humidity of zeolites on the energy storage density for different triangular honeycomb zeolite 13X configurations. A lower initial relative humidity of zeolites indicates drier zeolites during the charging process, resulting in greater stored heat energy. Consequently, this facilitates the release of more thermal energy and extends the discharging reaction time.

Figure 7. Energy storage for different triangular honeycomb zeolite 13X reactors. (**a**) $\varnothing_{ini,z} = 10\%$; (**b**) $\varnothing_{ini,z} = 7\%$; (**c**) $\varnothing_{ini,z} = 5\%$ and (**d**) $\varnothing_{ini,z} = 3\%$.

For the same initial relative humidity of triangular honeycomb zeolite 13X, a higher relative humidity of inlet air improves the energy storage density, particularly for the

triangular honeycomb reactor with angles of 60°, 60°, and 60°. The highest energy storage density of triangular honeycomb zeolite 13X is 872 kJ/kg under conditions of 3% initial relative humidity and 98% relative humidity of inlet air. However, at 10% initial relative humidity, the energy storage density for the triangular honeycomb reactor with angles of 60°, 60°, and 60° is slightly higher than at 7%, as the cumulative thermal energy is lower during the first hour of discharging but increases during the last hour as the adsorption reaction progresses. Additionally, the energy storage density of the triangular honeycomb reactor with angles of 30°, 60°, and 90° is generally higher than that of the triangular honeycomb reactor with angles of 45°, 45°, and 90°.

4.6. Reactor Round-Trip Thermal Efficiency

Thermal efficiency is a crucial parameter the evaluation of the feasibility of an entire thermochemical energy storage system, considering both the charging and discharging processes. Figure 8 shows the thermal efficiency of three different triangular honeycomb reactors under varying conditions of initial relative humidity of zeolites and relative humidity of inlet air. The thermal energy cumulated during the charging process shows minimal variation across reactors under different conditions of initial relative humidity. However, the thermal energy cumulated during the discharging process significantly impacts the thermal efficiency. The triangular honeycomb reactor with angles of 30°, 60°, and 90° achieves the highest thermal efficiency of 41.51% under conditions of 3% initial relative humidity and 98% relative humidity of inlet air.
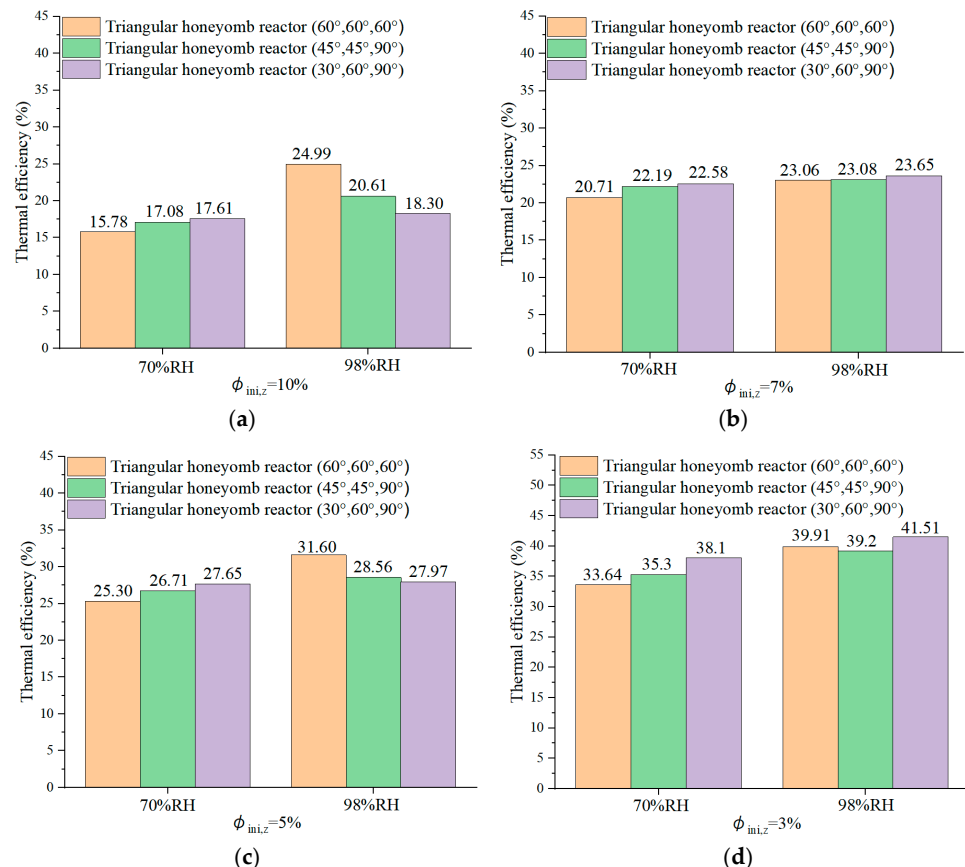
Figure 8. Thermal efficiency of different triangular honeycomb reactors. (**a**) $\varnothing_{ini,z} = 10\%$; (**b**) $\varnothing_{ini,z} = 7\%$; (**c**) $\varnothing_{ini,z} = 5\%$ and (**d**) $\varnothing_{ini,z} = 3\%$.

The higher relative humidity of inlet air also basically results in higher thermal efficiency for the triangular honeycomb reactor with angles of 60°, 60°, and 60° than that of the triangular honeycomb reactor with angles of 45°, 45°, and 90°.

4.7. The Feasibility of the Novel Reactor for a Typical Home in Northern China

This section provides insights with respect to the application of the proposed reactor in the context of residential heating. China, which is renowned for its vast population density, is confronted with significant challenges regarding energy consumption and greenhouse gas emissions, particularly in the realm of residential space heating in the northern regions. The magnitude of this issue underscores the urgent need for effective solutions to mitigate the strain on existing energy resources. The residential heating demand exceeds 963 million tons of standard coal equivalents (tce), accounting for 21% of the country's total energy consumption. These statistics highlight the urgent requirement for sustainable measures to reduce reliance on non-renewable energy sources. Low-carbon heating is also being widely studied and applied in many regions globally. Therefore, the high-level feasibility study presented in this section can also be adapted and applied to other regions.

With respect to a standard residential home in northern China, which typically has a gross internal floor area of 100 m^2, the focus is on the spatial efficiency of the reactor's volume dedicated to space heating. Referring to [36], Figure 9a presents the total heating energy requirement for a typical home throughout the heating season, which spans 150 days in representative northern Chinese cities. With these data, this study calculates the daily heating load for an example home and determines the required storage volume for the three triangular honeycomb reactor configurations, as shown in Figure 9b,c.
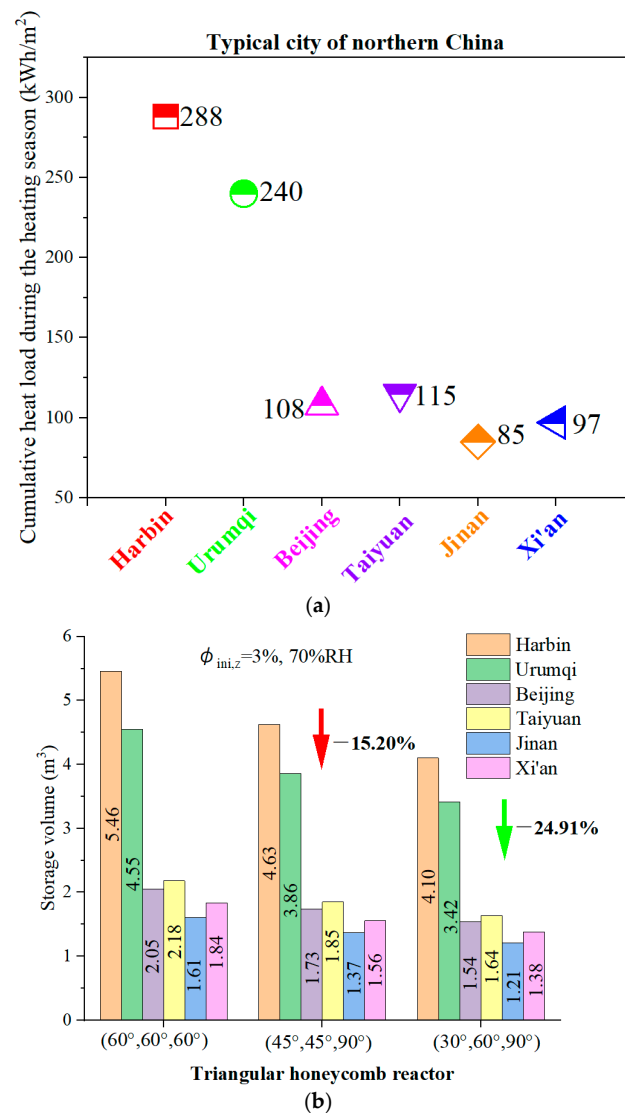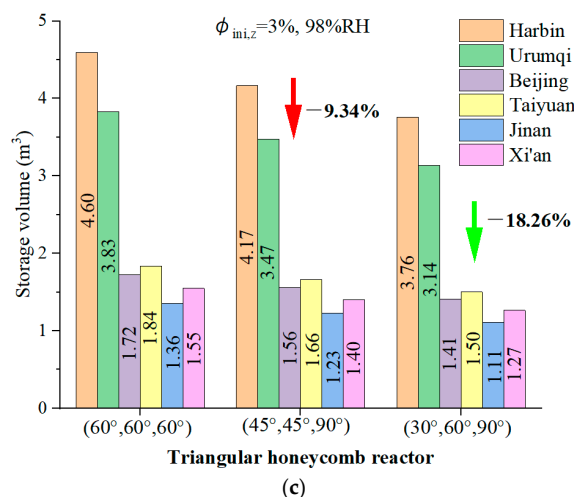

(a)

(b)

Figure 9. *Cont.*

Figure 9. (**a**) Aggregate heating energy demand for residential buildings within a typical northern Chinese city. (**b**,**c**) Capacity of triangular honeycomb reactors for heat storage.

As established in Section 4.5, the triangular honeycomb zeolite 13X variant exhibits superior energy storage density at a starting material humidity of 3%. This finding aligns with the volumetric energy storage performance of the triangular honeycomb reactor design. The analysis also reveals that the storage capacity of the triangular honeycomb reactor with 60° angles peaks at 5.46 m^3, assuming a relative humidity of inlet air of 70%. This capacity significantly exceeds that of reactors with angle configurations of 45°, 45°, and 90° and 30°, 60°, and 90°. Moreover, when compared with the reactor with angles of 60°, 60°, and 60°, the reactor with angles of 30°, 60°, and 90° has a 24.91% smaller required storage volume. This comparative study underscores the potential to optimize reactor design for enhanced energy storage in residential heating applications.

5. Conclusions

This study investigates a novel triangular honeycomb thermochemical energy storage reactor for medium- and low-temperature heating applications in buildings. The key findings of this research are summarized as follows:

- The triangular honeycomb reactor with angles of 60°, 60°, and 60° achieves an energy storage density of 872 kJ/kg and thermal efficiency of 39.91%.
- The reactor with angles of 30°, 60°, and 90° achieves a maximum air temperature lift of 48.7 °C during the discharging process, underlining its superior discharging capabilities, which are essential for efficient low-carbon building heating. Meanwhile, the configuration obtained the highest thermal efficiency of 41.51%.
- Pressure loss is a critical parameter in evaluating the thermal performance of a reactor. Pressure drop analysis showed that the reactor with angles of 60°, 60°, and 60° achieves the lowest pressure drop of 226.12 Pa/m, while the reactors with angles of 45°, 45°, and 90° and 30°, 60°, and 90° experience higher pressure drops of 430.55 Pa/m and 522.89 Pa/m, respectively.
- A feasibility study for residential heating in northern China demonstrated that the reactor with angles of 30°, 60°, and 90° requires 24.91% less volume to meet daily heating demands compared to the other designs, showcasing its compact and efficient energy storage potential.
- This study provides valuable insights into the optimization of reactors for flexible energy management, allowing for integration with renewable energy sources like solar power and off-peak electricity.

Data Availability Statement: The original contributions presented in the study are included in the article, further inquiries can be directed to the corresponding author.

Conflicts of Interest: The authors declare no conflict of interest.

Nomenclature

e	Side length (mm)		ρ	Density (kg/m^3)
C	Water concentration (mol/m^3)		$\varnothing$	Relative humidity (%)
c_p	Specific heat $(\text{J}/(\text{kg·K}))$		δ	Channel thickness (mm)
$D_\text{p,eff}$	Effective pore diffusion (m^2/s)		η	Thermal efficiency (%)
$D_\text{s,eff}$	Effective surface diffusion (m^2/s)		Subscripts	
$D_\text{v,a}$	Water vapor diffusivity in air (m^2/s)		a	Air
ΔH	Heat of adsorption (J/kg)		amb	Ambient
h	Specific enthalpy (J/kg)		char	Charging
$\dot{h}$	Thermal power (W)		cum	Cumulative
k	Thermal conductivity $(\text{W}/(\text{m·K}))$		dis	Discharging
k_LDF	Effective rate coefficient (1/s)		eff	Effective
L	Channel length (mm)		eq	Equilibrium
M	Molar mass (kg/mol)		exp	Experimental
m	Mass (kg)		ha	Humid air
$\dot{m}$	Air mass velocity (kg/h)		in/out	Inlet/outlet of the air channel
n	Vector (/)		ini	Initial
P	Pressure (Pa)		l	Liquid water
P_0	Atmospheric pressure (Pa)		p	Pores of zeolite
P_sat	Saturation pressure (Pa)		s	Surface
Q	Energy (J)		sim	Simulation
R	Universal gas constant $(\text{J}/(\text{mol·K}))$		tot	Entire adsorbent layer, including pores, the solid part, and adsorbed water vapor)
t	Time (s, h)		v	Water vapor
T	Temperature (K, °C)		w	Water
v	Velocity (m/s)		z	Zeolite matrix (exclude pores and adsorbed water vapor)
w_1	Water vapor content in the air (kg/kg)		zm	Matrix of zeolite (excluding zeolite pores)
w_2	Water vapor content in the pores of zeolite (kg/kg)		zp	Pores of zeolite (excluding zeolite matrix)
w	Water vapor content in the matrix of the adsorbent, $(\text{kg}_{water}/\text{kg}_{zeolite})$			
w_eq	Equilibrium adsorption amount $(\text{kg}_{water}/\text{kg}_{zeolite})$		Abbreviation	
			ESD	Energy storage density
Greek symbols			MSOPE	Mean sum of the percentage errors
ε	Porosity		RH	Relative humidity

References

1. Han, R.; Xing, S.; Wu, X.; Pang, C.; Lu, S.; Su, Y.; Liu, Q.; Song, C.; Gao, J. Relevant influence of alkali carbonate doping on the thermochemical energy storage of Ca-based natural minerals during $CaO/CaCO_3$ cycles. *Renew. Energy* **2022**, *181*, 267–277. [CrossRef]
2. Fopah Lele, A.; Kuznik, F.; Opel, O.; Ruck, W.K.L. Performance analysis of a thermochemical based heat storage as an addition to cogeneration systems. *Energy Convers. Manag.* **2015**, *106*, 1327–1344. [CrossRef]
3. Chao, J.; Xu, J.; Yan, T.; Wang, P.; Huo, X.; Wang, R.; Li, T. Enhanced thermal conductivity and adsorption rate of zeolite 13X adsorbent by compression-induced molding method for sorption thermal battery. *Energy* **2022**, *240*, 122797. [CrossRef]
4. Scapino, L.; Zondag, H.A.; Van Bael, J.; Diriken, J.; Rindt, C.C.M. Sorption heat storage for long-term low-temperature applications: A review on the advancements at material and prototype scale. *Appl. Energy* **2017**, *190*, 920–948. [CrossRef]
5. Zeng, C. Development and Investigation of a Novel Thermochemical Energy Storage Reactor for Residential Use. Ph.D. Thesis, Coventry University, Coventry, UK, 2020.

6. Feng, C.; E, J.; Han, W.; Deng, Y.; Zhang, B.; Zhao, X.; Han, D. Key technology and application analysis of zeolite adsorption for energy storage and heat-mass transfer process: A review. *Renew. Sustain. Energy Rev.* **2021**, *144*, 110954. [CrossRef]

7. Rönsch, S.; Auer, B.; Kinateder, M.; Gleichmann, K. Zeolite Heat Storage: Key Parameters from Experimental Results with Binder-Free NaY. *Chem. Eng. Technol.* **2020**, *43*, 2530–2537. [CrossRef]

8. Kant, K.; Pitchumani, R. Advances and opportunities in thermochemical heat storage systems for buildings applications. *Appl. Energy* **2022**, *321*, 119299. [CrossRef]

9. Michel, B.; Mazet, N.; Neveu, P. Experimental investigation of an open thermochemical process operating with a hydrate salt for thermal storage of solar energy: Local reactive bed evolution. *Appl. Energy* **2016**, *180*, 234–244. [CrossRef]

10. Weber, R.; Asenbeck, S.; Kerskes, H.; Drück, H. SolSpaces—Testing and Performance Analysis of a Segmented Sorption Store for Solar Thermal Space Heating. *Energy Procedia* **2016**, *91*, 250–258. [CrossRef]

11. Zhang, H.; Liu, S.; Shukla, A.; Zou, Y.; Han, X.; Shen, Y.; Yang, L.; Zhang, P.; Kusakana, K. Thermal performance study of thermochemical reactor using net-packed method. *Renew. Energy* **2022**, *182*, 483–493. [CrossRef]

12. Ji, W.; Zhang, H.; Liu, S.; Li, Y.; Wang, Z.; Deng, S. A metal mesh net-packed method for improving thermochemical energy storage reactor performance by increasing the void fraction. *Appl. Therm. Eng.* **2023**, *225*, 120248. [CrossRef]

13. Zeng, C.; Liu, S.; Yang, L.; Han, X.; Song, M.; Shukla, A. Investigation of a three-phase thermochemical reactor through an experimentally validated numerical modelling. *Appl. Therm. Eng.* **2019**, *162*, 114223. [CrossRef]

14. de Boer, R.; Smeding, S.F.; Zondag, H.A.; Krol, G. *Development of a Prototype System for Seasonal Solar Heat Storage Using an Open Sorption Process*; ECN: Petten, The Netherlands, 2014; pp. 28–30.

15. Tatsidjodoung, P.; Le Pierrès, N.; Heintz, J.; Lagre, D.; Luo, L.; Durier, F. Experimental and numerical investigations of a zeolite 13X/water reactor for solar heat storage in buildings. *Energy Convers. Manag.* **2016**, *108*, 488–500. [CrossRef]

16. van Alebeek, R.; Scapino, L.; Beving, M.A.J.M.; Gaeini, M.; Rindt, C.C.M.; Zondag, H.A. Investigation of a household-scale open sorption energy storage system based on the zeolite 13X/water reacting pair. *Appl. Therm. Eng.* **2018**, *139*, 325–333. [CrossRef]

17. Aydin, D.; Casey, S.P.; Chen, X.; Riffat, S. Novel "open-sorption pipe" reactor for solar thermal energy storage. *Energy Convers. Manag.* **2016**, *121*, 321–334. [CrossRef]

18. Casey, S.P.; Aydin, D.; Elvins, J.; Riffat, S. Salt impregnated desiccant matrices for 'open' thermochemical energy conversion and storage—Improving energy density utilisation through hygrodynamic & thermodynamic reactor design. *Energy Convers. Manag.* **2017**, *142*, 426–440. [CrossRef]

19. Zhang, Y.; Hu, M.; Chen, Z.; Su, Y.; Riffat, S. Exploring a novel tubular-type modular reactor for solar-driven thermochemical energy storage. *Renew. Energy* **2024**, *221*, 119767. [CrossRef]

20. Johannes, K.; Kuznik, F.; Hubert, J.-L.; Durier, F.; Obrecht, C. Design and characterisation of a high powered energy dense zeolite thermal energy storage system for buildings. *Appl. Energy* **2015**, *159*, 80–86. [CrossRef]

21. Han, X.; Zeng, C.; Liu, S.; Wang, Z.; Deng, S.; Zhang, H. Numerical study on the heat and mass transfer in charging and discharging processes of a triangular honeycomb thermochemical energy storage reactor. *Appl. Therm. Eng.* **2023**, *219*, 119499. [CrossRef]

22. Cheng, D.; Peters, E.A.J.F.; Kuipers, J.A.M. Performance study of heat and mass transfer in an adsorption process by numerical simulation. *Chem. Eng. Sci.* **2017**, *160*, 335–345. [CrossRef]

23. Zeng, C.; Liu, S.; Shukla, A.; Yang, L.; Han, X.; Shen, Y. Numerical modelling of the operational effects on the thermochemical reactor performance. *Energy Build.* **2021**, *230*, 110535. [CrossRef]

24. Cheng, D.; Peters, E.A.J.F.; Kuipers, J.A.M. Numerical modelling of flow and coupled mass and heat transfer in an adsorption process. *Chem. Eng. Sci.* **2016**, *152*, 413–425. [CrossRef]

25. Wang, W.; Pan, Q.; Wang, R.; Ge, T. Modeling and optimization of a honeycombed adsorbent bed for efficient moisture capture. *Appl. Therm. Eng.* **2022**, *200*, 117717. [CrossRef]

26. Kim, H.; Cho, H.J.; Narayanan, S.; Yang, S.; Furukawa, H.; Schiffres, S.; Li, X.; Zhang, Y.B.; Jiang, J.; Yaghi, O.M.; et al. Characterization of Adsorption Enthalpy of Novel Water-Stable Zeolites and Metal-Organic Frameworks. *Sci. Rep.* **2016**, *6*, 19097. [CrossRef]

27. Glueckauf, E. Theory of chromatography. Part 10. Formula for diffusion into spheres and their application to chromatography. *Trans. Faraday Soc.* **1955**, *51*, 1540–1551. [CrossRef]

28. Ruthven, D.M. *Principles of Adsorption and Desorption Processes*; John Wiley & Sons: New York, NY, USA, 1984.

29. Parsons, B.K.; Pesaran, A.A.; Bharathan, D.; Shelpuk, S. Evaluation of thermally activated heat pump/desiccant air conditioning systems and components. In *Evaluation of Thermally Activated Heat Pump/Desiccant Air Conditioning Systems and Components*; SERI/TR-252-3116; Oak Ridge National Laboratory: Oak Ridge, TN, USA, 1987.

30. Kuznik, F.; Gondre, D.; Johannes, K.; Obrecht, C.; David, D. Numerical modelling and investigations on a full-scale zeolite 13X open heat storage for buildings. *Renew. Energy* **2019**, *132*, 761–772. [CrossRef]

31. Ahn, H.; Lee, C.-H. Effects of capillary condensation on adsorption and thermal desorption dynamics of water in zeolite 13X and layered beds. *Chem. Eng. Sci.* **2004**, *59*, 2727–2743. [CrossRef]

32. Han, X.; Zeng, C.; Liu, S.; Cheng, Y.; Zhu, X. Maximizing Thermal Performance in Triangular Honeycomb Thermochemical Reactors: Structural and Operating Parameter Studies. *Energy* **2024**, *308*, 132743. [CrossRef]

33. Shukla, A.; Tiwari, G.N.; Sodha, M.S. Experimental study of effect of an inner thermal curtain in evaporative cooling system of a cascade greenhouse. *Sol. Energy* **2008**, *82*, 61–72. [CrossRef]

34. Allouche, Y.; Varga, S.; Bouden, C.; Oliveira, A.C. Validation of a CFD model for the simulation of heat transfer in a tubes-in-tank PCM storage unit. *Renew. Energy* **2016**, *89*, 371–379. [CrossRef]
35. Dolado, P.; Lazaro, A.; Marin, J.M.; Zalba, B. Characterization of melting and solidification in a real-scale PCM–air heat exchanger: Experimental results and empirical model. *Renew. Energy* **2011**, *36*, 2906–2917. [CrossRef]
36. Tang, J.; Sun, X.; Wang, P. Energy consumption analysis on the heating for different climates rural residential areas. *Heat. Vent. Air Cond.* **2022**, *52*, 37–41.